

Bright triplet excitons in lead halide perovskites

Michael A. Becker^{1,2,*}, Roman Vaxenburg^{3,*}, Georgian Nedelcu^{4,5}, Peter C. SerceI⁶, Andrew Shabaev³,
 Michael J. Mehl⁷, John G. Michopoulos⁸, Samuel G. Lambrakos⁸, Noam Bernstein⁸, John L. Lyons⁸,
 Thilo Stöferle¹, Rainer F. Mahrt¹, Maksym V. Kovalenko^{4,5}, David J. Norris², Gabriele Rainò^{1,4}, and
 Alexander L. Efros⁸

¹IBM Research – Zurich, Säumerstrasse 4, 8803 Rüschlikon, Switzerland.

²Optical Materials Engineering Laboratory, ETH Zurich, 8092 Zurich, Switzerland.

³Computational Materials Science Center, George Mason University, Fairfax, VA 22030 USA.

⁴Institute of Inorganic Chemistry, Department of Chemistry and Applied Bioscience, ETH Zurich, 8093 Zurich, Switzerland.

⁵Laboratory of Thin Films and Photovoltaics, Empa – Swiss Federal Laboratories for Materials Science and Technology, CH-8600 Dübendorf, Switzerland.

⁶T. J. Watson Laboratory of Applied Physics, California Institute of Technology, Pasadena, CA 91125 USA.

⁷U.S. Naval Academy, Annapolis, MD 21402 USA.

⁸Center for Computational Materials Science, Naval Research Laboratory, Washington, DC 20375 USA.

*These authors contributed equally to this work.

Nanostructured semiconductors emit light from electronic states known as excitons¹. For organic materials, Hund’s rules² state that the lowest energy exciton is a poorly emitting triplet state. For inorganic semiconductors, similar rules³ predict an analog of this triplet known as the ‘dark exciton’⁴. Because this state releases photons slowly, hindering emission from inorganic nanostructures, materials that disobey these rules have been sought. However, even after considerable experimental and theoretical efforts, no inorganic semiconductors have been identified in which the lowest exciton is bright. Here we show that the lowest exciton in cesium lead halide perovskites [CsPbX₃ (X = Cl, Br, and I)] involves a highly emissive triplet state. We first use the effective-mass model and group theory to explore this possibility, which can occur when the strong spin–orbit coupling in the perovskite conduction band is combined with the Rashba effect^{5–10}. We then apply our model to CsPbX₃ nanocrystals¹¹, for which we measure size- and composition-dependent fluorescence at the single-nanocrystal level. The bright-triplet character of the lowest exciton immediately explains the anomalous photon-emission rates of these materials, which emit ~20 and ~1,000 times faster¹² than any other semiconductor nanocrystal at room^{13–16} and cryogenic⁴ temperatures, respectively. The bright-triplet exciton is further confirmed by detailed analysis of the fine structure in low-temperature fluorescence spectra. For semiconductor nanocrystals, which are already used in lighting¹⁷, lasers¹⁸, and displays¹⁹, these excitons can lead to materials with brighter emission. More generally, our results provide criteria for identifying other semiconductors that exhibit bright excitons, with potential implications for optoelectronic devices.

An exciton involves an electron in the conduction band Coulombically bound to a hole in the valence band. Its energy depends in part on the spin configuration of these two charge carriers. In organic semiconductors, the lowest energy exciton is a triplet state in which these two carriers have parallel spins. For the electron and hole to recombine and release a photon, one spin must simultaneously flip to satisfy the Pauli exclusion principle. Because this coordinated process is unlikely, triplet excitons are poorly emitting.

In addition to spin, the exciton energy depends on the atomic orbitals that constitute the conduction and valence bands. In many inorganic semiconductors, the orbital motion and spin of the carriers are strongly coupled. Spin is no longer conserved, and the total angular momentum of the electron and hole (J_e and J_h) must be considered. Further, the exchange interaction mixes these so that only the total exciton momentum $\mathbf{J}=\mathbf{J}_e+\mathbf{J}_h$ is conserved. Due to these and other effects, each exciton state is split into several energy sublevels, known as fine structure. Studies on various materials have found that the lowest energy sublevel is 'dark', meaning that optical transitions to the ground state are dipole forbidden. Emission, if it occurs, is very slow. For example, in CdSe, recombination of the lowest exciton requires a change of two units of angular momentum⁴. Because the photon carries one unit, light cannot be emitted unless another unit is simultaneously dissipated, another unlikely process. The lowest exciton in all known inorganic semiconductors behaves similarly, leading to the common belief that such states *must* be dark.

We show that this belief is incorrect by examining CsPbX₃ (X=Cl, Br, and I) perovskites. Their crystals comprise corner-sharing PbX₆-octahedra with Cs⁺ ions filling the voids between (Fig. 1a). We first approximate the lattice as cubic and calculate band structures (Methods) for CsPbBr₃ (Fig. 1b), CsPbCl₃, and CsPbI₃ (Extended Data Fig. 1). The bandgap occurs at the Brillouin zone's R-point, near which the valence and conduction bands are well described

63 within the effective-mass model (see Supplementary Table 1). The top of the valence band
 64 arises from a mixture of Pb 6s and Br 4p atomic orbitals, with an overall s symmetry^{20,21}.
 65 Thus, including spin, the hole can occupy one of two s-like Bloch states with $J_h=1/2$, *i.e.*
 66 $|\uparrow\rangle_h = |S\rangle|\uparrow\rangle$ or $|\downarrow\rangle_h = |S\rangle|\downarrow\rangle$, using standard notation²². The conduction band consists of Pb
 67 6p orbitals, leading to three possible orthogonal spatial components for the Bloch function:
 68 $|X\rangle$, $|Y\rangle$, or $|Z\rangle$ ^{20,21}. Because of strong spin–orbit coupling, these are mixed with spin to obtain
 69 a doubly degenerate $J_e=1/2$ state for the electron at the bottom of the conduction band:

$$\begin{aligned} |\uparrow\rangle_e &= -\frac{1}{\sqrt{3}} [(|X\rangle + i|Y\rangle)|\downarrow\rangle + |Z\rangle|\uparrow\rangle], \\ |\downarrow\rangle_e &= \frac{1}{\sqrt{3}} [|Z\rangle|\downarrow\rangle - (|X\rangle - i|Y\rangle)|\uparrow\rangle]. \end{aligned} \quad (1)$$

71 When the momentum of the electron and hole states are then combined, the exciton splits
 72 due to electron–hole exchange into a $J=0$ singlet state,

$$|\Psi_{0,0}\rangle = \frac{1}{\sqrt{2}} [|\downarrow\rangle_e |\uparrow\rangle_h - |\uparrow\rangle_e |\downarrow\rangle_h], \quad (2)$$

74 and a threefold degenerate $J=1$ triplet state,

$$|\Psi_{1,-1}\rangle = |\downarrow\rangle_e |\downarrow\rangle_h, |\Psi_{1,0}\rangle = \frac{1}{\sqrt{2}} [|\downarrow\rangle_e |\uparrow\rangle_h + |\uparrow\rangle_e |\downarrow\rangle_h], |\Psi_{1,+1}\rangle = |\uparrow\rangle_e |\uparrow\rangle_h, \quad (3)$$

76 where each $|\Psi_{J,J_z}\rangle$ is labeled with J_z , the z-projection of J . The probability of light emission
 77 due to electron–hole recombination from these excitons can then be calculated
 78 (Supplementary Section 1). We find a probability of zero for $|\Psi_{0,0}\rangle$ and nonzero for $|\Psi_{1,J_z=0,\pm 1}\rangle$,
 79 indicating a dark singlet and bright triplet.

80 These selection rules are confirmed by group theory. At the R-point, the band-edge
 81 electron and hole states transform as irreducible representations R_6^- and R_6^+ , respectively
 82 (superscript denoting parity)²³. Exchange then splits the exciton into a dark singlet (R_1^-) and a
 83 bright triplet (R_4^-). (See Supplementary Section 2 and Supplementary Table 3.)

84 Detailed calculations (Supplementary Section 1) can then reveal the energetic order of
85 these levels. If only short-range exchange is included, the singlet lies below the triplet (Fig.
86 1c). However, CsPbX₃ perovskites should also exhibit a large Rashba effect⁵. This occurs in
87 semiconductors with strong spin–orbit coupling and an inversion asymmetry. For the closely
88 related hybrid organic–inorganic perovskites, the impact of this effect on photovoltaic and
89 spintronic devices has been heavily discussed^{6–9}. Although the cause of the inversion
90 asymmetry (cation positional instabilities²⁴ or surface effects⁹) remains unknown, the Rashba
91 effect should alter the fine structure. Indeed, the bright triplet exciton can be lowered below
92 the dark singlet exciton.

93 To examine this possibility, we studied colloidal nanocrystals of CsPbX₃ (Methods).
94 Compared to bulk crystals, nanocrystals allow the additional effect of system size to be
95 investigated. Such particles are roughly cube-shaped with edge lengths $L=8\text{--}15\text{ nm}$ (Fig. 1d).
96 Before these were introduced¹¹, all technologically relevant semiconductor nanocrystals
97 exhibited slow sub-microsecond radiative lifetimes at cryogenic temperatures due to the
98 lowest exciton being dark⁴. In contrast, CsPbX₃ nanocrystals emit $\sim 1000\times$ faster (with sub-
99 nanosecond lifetimes)¹². Figure 2a shows photoluminescence decays for individual CsPbI₃,
100 CsPbBr₃, and CsPbBr₂Cl nanocrystals at cryogenic temperatures. The decay times are 0.85,
101 0.38, and 0.18 ns, respectively, decreasing with increasing emission energy. The
102 photoluminescence quantum yield for the fastest of these samples, the CsPbBr₂Cl
103 nanocrystals ($L=14\pm 1\text{ nm}$), was measured to be near unity ($88\pm 14\%$) at 5 K (Extended Data
104 Fig. 2), indicating that these decay times can be directly related to radiative lifetimes. Figure
105 2b presents a larger set of decay times (squares) for individual CsPbI₃, CsPbBr₃, and
106 CsPbBr₂Cl nanocrystals. All are much shorter than those reported for CdSe, CdS, CdTe,

107 InAs, InSb, InP, PbSe, PbS, and PbTe nanocrystals¹³⁻¹⁶, consistent with the lowest exciton
108 being the bright triplet.

109 However, fast decays could also indicate emission from trions (charged excitons). Trions
110 are optically active but suffer from rapid nonradiative Auger recombination. Thus, they should
111 exhibit quicker but weaker decays than excitons. In our single-nanocrystal experiments
112 above, trion contributions are reduced by spectral filtering (Extended Data Fig. 3). However,
113 to test explicitly the role of trions, we analyzed the photon stream from individual nanocrystals
114 without filtering (Fig. 2c,d, left plots). The correlation of emission intensity with lifetime allows
115 the strong exciton and weak trion contributions to be separated (right plots)²⁵. We confirm fast
116 exciton lifetimes (1.2 and 0.4 ns, respectively) for CsPbI₃ and CsPbBr₃ nanocrystals, values
117 consistent with ensemble measurements (Extended Data Fig. 4).

118 To compare with theory, we calculated radiative lifetimes for perovskite nanocrystals
119 within the effective-mass model. In addition to the wavefunctions in equations (2)-(3), exciton
120 confinement within the nanocrystal must be included via envelope functions for the electron
121 and hole. If CsPbX₃ nanocrystals were spherical, excitonic lifetimes could be calculated with
122 prior methods (Supplementary Section 3). However, for cubes, the electric field of a photon
123 not only changes across the nanocrystal boundary due to dielectric screening (as in spherical
124 nanocrystals), but it also becomes inhomogeneous (Fig. 2e and Extended Data Figs. 5 and
125 6). We included this inhomogeneity, along with the Rashba effect and the orthorhombic lattice
126 distortion in CsPbX₃ nanocrystals²⁶. For simplicity, we assumed the nanocrystals were cube
127 shaped. Only when the Rashba effect was included could a self-consistent model for CsPbX₃
128 nanocrystals be obtained, as now described.

129 The Rashba coefficient was estimated from low-temperature photoluminescence spectra
130 (see below). If the effective Rashba field is parallel to one of the orthorhombic symmetry axes

131 of the nanocrystal (see Supplementary Section 1 for details and other cases), the bright triplet
 132 exciton ($J=1$) is split into three nondegenerate sublevels:

$$133 \quad |\Psi_x\rangle = \frac{1}{\sqrt{2}} [|\uparrow\rangle_e |\uparrow\rangle_h - |\downarrow\rangle_e |\downarrow\rangle_h], \quad |\Psi_z\rangle = |\Psi_{1,0}\rangle, \quad |\Psi_y\rangle = \frac{1}{\sqrt{2}} [|\uparrow\rangle_e |\uparrow\rangle_h + |\downarrow\rangle_e |\downarrow\rangle_h], \quad (4)$$

134 which lie below the dark singlet (Fig. 1c). The triplet states represent three linear dipoles
 135 polarized along the orthorhombic symmetry axes (x , y , z). Transitions from these three
 136 sublevels have the same oscillator strength. Moreover, in cube-shaped nanocrystals, these
 137 states still emit as linear dipoles despite the inhomogeneous field (Supplementary Sections 1
 138 and 3).

139 The triplet exciton radiative lifetime, τ_{ex} , can then be evaluated from:

$$140 \quad \frac{1}{\tau_{ex}} = \frac{4\omega n E_p}{9 \times 137 m_0 c^2} I_{\parallel}^2. \quad (5)$$

141 with the angular transition frequency, ω , the refractive index of the surrounding medium, n , the
 142 free-electron mass, m_0 , the speed of light, c , the Kane energy, $E_p = 2P^2/m_0$ (Extended Data
 143 Fig. 7), and the Kane parameter, P (ref. 22). I_{\parallel} is an overlap integral that includes the electron
 144 and hole envelope functions and the field-averaged transition-dipole moment (Supplementary
 145 Section 3).

146 Figure 2b presents the calculated τ_{ex} for CsPbX₃ nanocrystals (circles). The results can
 147 be divided into three regimes, depending on the nanocrystal size. When the nanocrystal is
 148 smaller than the exciton Bohr radius a_B (strong exciton confinement, orange circles), the
 149 predicted radiative lifetime decreases from 2 to 1 ns with increasing emission energy. For
 150 large nanocrystals in the opposite limit (weak exciton confinement, green circles), the lifetime
 151 should be even shorter as weakly confined excitons exhibit larger oscillator strengths²⁷. In this
 152 size regime ($L \sim 15$ -25 nm), the calculated lifetimes decrease below 100 ps for CsPbBr₃ and

153 CsPbCl₃ nanocubes. The lifetime would be decreased further in spheres of the same volume
154 (lower inset, Fig. 2e).

155 The measured photoluminescence decays in Fig. 2b (squares) lie between those
156 predicted for strong and weak confinement. Because the nanocrystal size and a_B are
157 comparable, the electron and hole motion is correlated. If this effect is added (intermediate
158 exciton confinement, blue circles), calculations for $L \sim 4\text{-}16$ nm (Supplementary Section 3 and
159 Extended Data Fig. 8) agree well with experiment.

160 The exciton level order used above depends on the values and relative signs of the
161 Rashba coefficients for the electron and hole. If they have the same sign, the angular-
162 momentum texture (*i.e.* how the angular-momentum orientation varies with wavevector)
163 exhibits the same helicity at the valence band maximum and conduction band minimum⁷.
164 Optical transitions between these bands are allowed when the helicity is preserved (due to
165 their *s* and *p* symmetry, respectively.) Thus, for this case, the lowest exciton sublevel should
166 be bright. See Supplementary Section 1.E for details. A similar situation exists in transition
167 metal dichalcogenide monolayers²⁸.

168 We estimated the values of the Rashba coefficients from photoluminescence spectra of
169 individual nanocrystals, which reveal the fine structure directly. Our nanocrystals exhibit one,
170 two, or three peaks, all with near-linear polarization (Fig. 3a-c and Extended Data Figs. 9 and
171 10). This is consistent with the three nondegenerate exciton sublevels in equation (4) under
172 orthorhombic symmetry, which should emit as orthogonal linear dipoles. For simplicity, we
173 assume that the electron and hole Rashba coefficients are equal. The value (0.38 eV Å)
174 required to fit the observed splittings (~ 1 meV) is reasonable, lying between those for
175 conventional III-V quantum wells and organic–inorganic perovskites (see Supplementary
176 Section 1.F). We note that for nanocrystals with tetragonal symmetry, $|\Psi_x\rangle$ and $|\Psi_y\rangle$ in

equation (4) remain degenerate (Supplementary Section 1.E), explaining recently observed two-peak spectra from individual CsPbBr₃ nanocrystals²⁹.

Emitting dipoles that are perpendicular (parallel) to the observation direction should show strong (no) emission. Thus, the intensity from each bright-triplet sublevel is explained by both its thermal population and the nanocrystal orientation. Single-line spectra (Fig. 3a) arise when the two upper sublevels are unpopulated. Strong linear polarization from this single line (Fig. 3a, inset) supports this interpretation. If the sublevel splitting in this nanocrystal were instead spectrally unresolved, the line would be unpolarized. From the expected three orthogonal dipoles, we calculated the relative intensity of the photoluminescence peaks and their polarization for arbitrary observation directions (Supplementary Section 4 and Extended Data Fig. 11). We then determined (Fig. 3d-f) the nanocrystal orientations consistent with the spectra and polarizations in Fig. 3a-c. Again, good agreement is obtained.

Figure 3g presents the experimental statistics for one-, two-, and three-line spectra. One is most common, suggesting that only the lowest sublevel is populated. For the two- and three-line spectra, the measured energy splittings are plotted in Fig. 3h,i. Given three sublevels separated by energies Δ_1 and Δ_2 (inset, Fig. 3i), the average splitting $\bar{\Delta}$ is $0.5(\bar{\Delta}_1 + \bar{\Delta}_2)$, bars denoting averages. However, two-line spectra can involve any two of the three features, leading to the average $\bar{\Delta}_1/3 + \bar{\Delta}_2/3 + (\bar{\Delta}_1 + \bar{\Delta}_2)/3 = 2(\bar{\Delta}_1 + \bar{\Delta}_2)/3$. Thus, we predict a ratio of 1.33 for average measured splittings in two- versus three-line spectra. The experimental ratio of 1.42 ± 0.12 again supports our model.

While we have used cryogenic temperatures to confirm the bright triplet exciton, it remains important at room temperature. Although the splittings are small compared to thermal energy, the three triplet states (from four sublevels in total) are dipole allowed and thermally populated, unlike in other nanocrystals¹³⁻¹⁶. For example, in CdSe nanocrystals only 3 of 8

band-edge sublevels are bright, and these can be poorly populated even at room temperature. This and other effects (Supplementary Section 5) explain why room-temperature emission from CsPbX₃ perovskite nanocrystals is 20x faster than in other systems. The emission should be even faster for nanowires and nanoplatelets. Such shapes can further decrease the radiative lifetime due to diminished dielectric screening and smaller one- or two-dimensional excitons³⁰.

Although CsPbX₃ nanocrystals are oxidatively stable, their long-term stability may be limited in warm, bright, and moist environments without encapsulation that prevents sintering and provides environmental stability. Moreover, the discovery that their lowest exciton is bright reveals criteria for obtaining this phenomenon in other materials. Potential semiconductors should lack inversion symmetry, and one band edge should have s symmetry and the other *p*, with the latter affected by strong spin–orbit coupling such that $J_{e,h}=1/2$. Finally, the Rashba coefficient for both bands must be nonzero with the same sign.

Online Content Methods, along with any Extended Data display items and Source Data, are available in the online version of the paper; references unique to these sections appear only in the online paper.

1. Scholes, G. D. & Rumbles, G. Excitons in nanoscale systems. *Nat. Mater.* **5**, 683-696 (2006).
2. Hund, F. Concerning the interpretation of complex spectra, especially the elements scandium to nickel. *Z. Phys.* **33**, 345-371 (1925).
3. Onodera, Y. & Toyozawa, Y. Excitons in alkali halides. *J. Phys. Soc. Jpn.* **22**, 833-844 (1967).
4. Nirmal, M., Norris, D. J., Kuno, M., Bawendi, M. G., Efros, A. L. & Rosen, M. Observation of the 'dark exciton' in CdSe quantum dots. *Phys. Rev. Lett.* **75**, 3728-3731 (1995).
5. Bychkov, Yu. A. & Rashba, E. I. Oscillatory effects and the magnetic susceptibility of carriers in inversion layers. *J. Phys. C: Solid State Phys.* **17**, 6039-6045 (1984).
6. Kim, M., Im, J., Freeman, A. J., Ihm, J. & Jin, H. Switchable $S = 1/2$ and $J = 1/2$ Rashba bands in ferroelectric halide perovskites. *Proc. Natl. Acad. Sci.* **111**, 6900-6904 (2014).
7. Zheng, F., Tan, L. Z., Liu, S. & Rappe, A. M. Rashba spin–orbit coupling enhanced carrier lifetime in CH₃NH₃PbI₃. *Nano Lett.* **15**, 7794-7800 (2015).
8. Kepenekian, M., Robles, R., Katan, C., Saporì, D., Pedesseau, L. & Even, J. Rashba and Dresselhaus effects in hybrid organic–inorganic perovskites: From basics to devices. *ACS Nano* **9**, 11557-11567 (2015).

9. Mosconi, E., Etienne, T. & De Angelis, F. Rashba band splitting in organohalide lead perovskites: Bulk and surface effects. *J. Phys. Chem. Lett.* **8**, 2247-2252 (2017).
10. Isarov, M., Tan, L. Z., Bodnarchuk, M. I., Kovalenko, M. V., Rappe, A. M. & Lifshitz, E. Rashba effect in a single colloidal CsPbBr₃ perovskite nanocrystal detected by magneto-optical measurements. *Nano Lett.* **17**, 5020-5026 (2017).
11. Protesescu, L., Yakunin, S., Bodnarchuk, M. I., Krieg, F., Caputo, R., Hendon, C. H., Yang, R. X., Walsh, A. & Kovalenko, M. V. Nanocrystals of cesium lead halide perovskites (CsPbX₃, X = Cl, Br, and I): Novel optoelectronic materials showing bright emission with wide color gamut. *Nano Lett.* **15**, 3692-3696 (2015).
12. Rainò, G., Nedelcu, G., Protesescu, L., Bodnarchuk, M. I., Kovalenko, M. V., Mahrt, R. F. & Stöferle, T. Single cesium lead halide perovskite nanocrystals at low temperature: Fast single-photon emission, reduced blinking, and exciton fine structure. *ACS Nano* **10**, 2485-2490 (2016).
13. Crooker, S. A., Barrick, T., Hollingsworth, J. A. & Klimov, V. I. Multiple temperature regimes of radiative decay in CdSe nanocrystal quantum dots: Intrinsic limits to the dark-exciton lifetime. *Appl. Phys. Lett.* **82**, 2793-2795 (2003).
14. Wuister, S. F., van Houselt, A., de Mello Donegá, C., Vanmaekelbergh, D. & Meijerink, A. Temperature anti-quenching of the luminescence from capped CdSe quantum dots. *Angew. Chem.* **43**, 3029-3033 (2004).
15. Du, H., Chen, C., Krishnan, R., Krauss, T. D., Harbold, J. M., Wise, F. W., Thomas, M. G. & Silcox, J. Optical properties of colloidal PbSe nanocrystals. *Nano Lett.* **2**, 1321-1324 (2002).
16. Bischof, T. S., Correa, R. E., Rosenberg, D., Dauler, E. A. & Bawendi, M. G. Measurement of emission lifetime dynamics and biexciton emission quantum yield of individual InAs colloidal nanocrystals. *Nano Lett.* **14**, 6787-6791 (2014).
17. Shirasaki, Y., Supran, G. J., Bawendi, M. G. & Bulovic, V. Emergence of colloidal quantum-dot light-emitting technologies. *Nature Photon.* **7**, 13-23 (2013).
18. Dang, C., Lee, J., Breen, C., Steckel, J. S., Coe-Sullivan, S. & Nurmikko, A. Red, green and blue lasing enabled by single-exciton gain in colloidal quantum dot films. *Nat. Nanotechnol.* **7**, 335-339 (2012).
19. Kim, T. H., Cho, K. S., Lee, E. K., Lee, S. J., Chae, J., Kim, J. W., Kim, D. H., Kwon, J. Y., Amaratunga, G., Lee, S. Y., Choi, B. L., Kuk, Y., Kim, J. M. & Kim, K. Full-colour quantum dot displays fabricated by transfer printing. *Nature Photon.* **5**, 176-182 (2011).
20. Bir, G. L. & Pikus, G. E., *Symmetry and Strain-Induced Effects in Semiconductors*. (Wiley, New York, 1974).
21. Even, J., Pedesseau, L., Jancu, J.-M. & Katan, C. Importance of spin-orbit coupling in hybrid organic/inorganic perovskites for photovoltaic applications. *J. Phys. Chem. Lett.* **4**, 2999-3005 (2013).
22. Kane, E. O. in *Semiconductors and Semimetals*, edited by R. K. Willardson and A. C. Beer (Academic Press, New York, 1966), Vol. 1, pp. 75-100.
23. Koster, G. F., Dimmock, J. O., Wheeler, R. G. & Statz, H., *Properties of the Thirty-Two Point Groups*. (MIT Press, Cambridge, 1963).
24. Yaffe, O., Guo, Y., Tan, L. Z., Egger, D. A., Hull, T., Stoumpos, C. C., Zheng, F., Heinz, T. F., Kronik, L., Owen, J. S., Rappe, A. M., Pimenta, M. A. & Brus, L. E. Local polar fluctuations in lead halide perovskite crystals. *Phys. Rev. Lett.* **118**, 136001 (2017).
25. Galland, C., Ghosh, Y., Steinbruck, A., Sykora, M., Hollingsworth, J. A., Klimov, V. I. & Htoon, H. Two types of luminescence blinking revealed by spectroelectrochemistry of single quantum dots. *Nature* **479**, 203-207 (2011).
26. Cottingham, P. & Brutchey, R. L. On the crystal structure of colloidally prepared CsPbBr₃ quantum dots. *Chem. Commun.* **52**, 5246-5249 (2016).
27. Rashba, E. I. & Gurgenishvili, G. E. Edge absorption theory in semiconductors. *Sov. Phys. Solid State* **4**, 759-760 (1962).
28. Dery, H. & Song, Y. Polarization analysis of excitons in monolayer and bilayer transition-metal dichalcogenides. *Phys. Rev. B* **92**, 125431 (2015).

- 284 29. Fu, N.; Tamarat, P.; Huang, H.; Even, J.; Rogach, A. L.; Lounis, B. Neutral and charged exciton
285 fine structure in single lead halide perovskite nanocrystals revealed by magneto-optical
286 spectroscopy. *Nano Lett.* **17**, 2895-2901 (2017).
287 30. Rodina, A. V. & Efros, Al. L. Effect of dielectric confinement on optical properties of colloidal
288 nanostructures. *J. Exp. Theor. Phys.* **122**, 554-566 (2016).
289

290 **Supplementary Information** is available in the online version of the paper.

291 **Acknowledgements** We thank F. Krieg for providing large CsPbBr₃ nanocrystals, S. Yakunin
292 and J. Jagielski for assistance with absolute quantum-yield measurements, and E. Ivchenko,
293 M. Glazov, and E. Rashba for useful discussions. M.A.B., G.R., T.S., M.V.K., and R.F.M.
294 acknowledge the European Union's Horizon-2020 programme through the Marie-Sklodowska
295 Curie ITN network PHONSI (H2020-MSCA-ITN-642656) and the Swiss State Secretariat for
296 Education Research and Innovation (SERI). J.G.M., S.G.L., N.B., J.L.L., and Al.L.E.
297 acknowledge support from the U.S. Office of Naval Research (ONR) through the core funding
298 of the Naval Research Laboratory. R.V. was funded by ONR Grant N0001416WX01849. A.S.
299 acknowledges support from the Center for Advanced Solar Photophysics (CASP), an Energy
300 Frontier Research Center (EFRC) funded by BES, OS, U.S. DOE. D.J.N. and M.V.K.
301 acknowledge partial financial support from the European Research Council under the
302 European Union's Seventh Framework Program (FP/2007-2013) / ERC Grant Agreement Nr.
303 339905 (QuaDoPS Advanced Grant) and Nr. 306733 (NANOSOLID Starting Grant),
304 respectively.

305 **Author contributions** This work resulted from ongoing interactions between G.R., M.V.K.,
306 D.J.N., and Al.L.E. M.A.B., G.R., and T.S. performed the optical experiments. They analyzed
307 and interpreted the data with input from D.J.N., R.F.M., P.C.S., and Al.L.E. Al.L.E. conceived
308 the model and supervised the theoretical research. R.V. calculated the radiative lifetimes and
309 developed theory for the observed exciton fine structure. R.V. and A.S. developed the 4-band

310 model describing the energy dispersion at the R-point and calculated the fine structure using
311 the wavefunction extracted from first-principle calculations. P.C.S. performed the group-theory
312 analysis of the fine structure and selection rules. M.J.M., N.B., and J.L.L. completed the first-
313 principle calculations of the bulk band structures and the band-edge wavefunctions. R.V.,
314 P.C.S, and Al.L.E. developed the effective exchange and Rashba Hamiltonian describing the
315 exciton fine structure. J.G.M. and S.G.L. calculated the internal electric fields in spherical and
316 cube-shaped nanocrystals. G.N. prepared the samples and performed electron microscopy
317 under the supervision of M.V.K. Al.L.E. and D.J.N. wrote the manuscript with input from all
318 authors.

319 **Author Information** The authors declare no competing financial interests. Readers are
320 welcome to comment on the online version of the paper. Correspondence and requests for
321 materials should be addressed to M.V.K. (mvkovalenko@ethz.ch), G.R. (rainog@ethz.ch),
322 D.J.N. (dnorris@ethz.ch), or Al.L.E. (sasha.efros@nrl.navy.mil).

323

324 **Figure legends**

325 **Figure 1 | Crystal and electronic structure for perovskite CsPbBr₃.** **a**, Orthorhombic
326 crystal structure of CsPbBr₃ (Pnma space group, unit cell shown as a frame), which differs
327 from the idealized cubic perovskite by an octahedral tilting. **b**, Calculated band structure of
328 cubic perovskite CsPbBr₃. The inset shows the first Brillouin zone of the cubic crystal lattice.
329 **c**, The expected fine structure of the band-edge exciton considering short-range electron–
330 hole exchange (middle) and then including the Rashba effect (right) under orthorhombic
331 symmetry. The latter splits the exciton into three bright states with transition dipoles oriented
332 along the orthorhombic symmetry axes (labelled x, y, and z) and a higher energy dark state.

333 The energetic order of the three lower sublevels is determined by the orthorhombic distortion.
334 The orthorhombic unit cell and the resulting sublevel order is shown for CsPbBr₃. **d**,
335 Transmission electron micrograph of an individual CsPbBr₃ nanocrystal of edge length $L=14$
336 nm.

337 **Figure 2 | Characterization of fast radiative lifetimes in CsPbX₃ nanocrystals. a**,
338 Photoluminescence decays measured from single CsPbI₃ ($L=14$ nm), CsPbBr₃ (11 nm), and
339 CsPbBr₂Cl (14 nm) perovskite nanocrystals. **b**, Calculated radiative lifetimes of the bright
340 triplet exciton versus transition energy for CsPbX₃ nanocrystals with X=Cl, Br, and I. The
341 theoretical results are divided into three size regimes: strong (orange circles), intermediate
342 (blue circles), and weak (green circles) exciton confinement. These values are compared with
343 measured photoluminescence decays from individual perovskite nanocrystals (squares, sizes
344 as in **a**). A data point for an ensemble of CsPbCl₃ nanocrystals ($L=10$ nm) is also shown.
345 Measured values are consistent with calculations in the intermediate confinement regime,
346 which include electron–hole correlations. **c,d** Detected photon counts (left panels) versus time
347 from individual CsPbI₃ and CsPbBr₃ nanocrystals (sizes as in **a**). Traces show “A-type”
348 blinking from the nanocrystals²⁵. Such data can be analyzed to separate contributions to the
349 photoluminescence decay from exciton and trion emission (right panel). The targeted
350 temperature in all experiments was 5 K, but may be higher (10-20 K; see Fig. 3 caption). **e**,
351 Calculated distribution of the z component of the electric field, E_z^z , normalized to the applied
352 field (along the z direction) at infinite distance, E_∞^z , *i.e.* E_z^z/E_∞^z . This quantity is plotted versus
353 position z across the center line of spherical (dashed lines) or cube-shaped (solid lines)
354 nanocrystals for various ratios of the dielectric constant inside (ϵ_{in}) to outside (ϵ_{out}) the
355 nanocrystal. The field inside the nanocrystal is essentially always lower for the cube
356 compared to the sphere. Upper inset: Calculated two-dimensional distribution of E_z^z/E_∞^z inside

357 a cube-shaped nanocrystal plotted on the xz mid-plane. The ratio $\epsilon_{\text{in}}/\epsilon_{\text{out}}$ was 6. Lower inset:
358 Calculated ratio of radiative decay times for spherical and cubical nanocrystals with the same
359 volume versus $\epsilon_{\text{in}}/\epsilon_{\text{out}}$ for strong and weak confinement.

360 **Figure 3 | Fine structure of the bright triplet exciton for CsPbBr₂Cl nanocrystals. a-c,**
361 Photoluminescence spectra of individual nanocrystals ($L=14\pm1$ nm) exhibiting a single peak,
362 two peaks, and three peaks. The targeted temperature was 5 K. However, a quantitative fit of
363 the peaks based on a Boltzmann distribution required higher (10-20 K) temperatures. This
364 may indicate a warmer sample temperature due to imperfect thermal contact and/or laser
365 heating. Alternatively, deviations from a Boltzmann distribution may be present. The inset
366 shows the polarization of each of the spectral features. For the spectra, a linear polarizer was
367 placed in the detection path. The angle of this polarizer was adjusted such that the relative
368 intensity of the features in the spectra matched the polarization dependence in the insets. **d-f,**
369 Simulated spectra and polarizations for nanocrystal orientations that match the experimental
370 results in **a-c**. See Supplementary Section 4 for details. Each panel lists the observation
371 direction required relative to the orthorhombic unit-cell axes. **g**, Experimental statistics for
372 observation of single-peak, two-peak, and three-peak spectra from individual nanocrystals
373 with $L=7.5$ -14 nm (51 spectra with 35 splittings in total). **h,i** Experimental fine-structure
374 splitting measured for the two-peak and three-peak spectra, respectively. The average
375 splitting in each case is provided.

376 **Methods**

377 **Chemicals.** The following reagents were used to prepare CsPbX₃ nanocrystals: cesium
378 carbonate (Cs₂CO₃, Aldrich, 99.9%), 1-octadecene (ODE, Sigma-Aldrich, 90%), oleic acid
379 (OA, Sigma-Aldrich, 90%), oleylamine (OAm, Acros Organics, 80-90%), lead chloride (PbCl₂,

380 ABCR, 99.999%), lead bromide (PbBr_2 , ABCR, 98%), lead iodide (PbI_2 , ABCR, 99.999%), n-
381 trioctylphosphine (TOP, Strem, 97%), hexane (Sigma-Aldrich, $\geq 95\%$), and toluene (Fischer
382 Scientific, HPLC grade).

383 **Synthesis.** The CsPbX_3 ($\text{X}=\text{Cl}$, Br , and I) and CsPbBr_2Cl nanocrystals were synthesized by
384 fast reaction between Cs-oleate and PbX_2 in the presence of OA and OAm (TOP is also
385 added for CsPbCl_3 and CsPbBr_2Cl nanocrystals). First, the Cs-oleate was prepared by
386 loading Cs_2CO_3 (0.407 g) into a 50-ml 3-neck flask along with ODE (20 ml) and OA (1.25 ml).
387 The mixture is dried under vacuum for 1 h at 120°C and then switched to N_2 . Since Cs-oleate
388 precipitates out of ODE at room temperature, it must be pre-heated to 100°C before injection.
389 The ODE, OA, and OAm were pre-dried before use by degassing under vacuum at 120°C for
390 1 h. For the nanocrystal reaction, 0.376 mmol PbX_2 ($\text{X}=\text{Cl}$, Br , or I), dried OA (3 ml for
391 PbCl_2 , 1 ml for PbBr_2 , or 1.5 ml for PbI_2), dried OAm (3 ml for PbCl_2 , 1 ml for PbBr_2 , or 1.5 ml
392 for PbI_2), and dried ODE (5 ml) were combined in a 25-ml 3-neck flask. For CsPbCl_3 , TOP (1
393 ml) was also added. The mixture was then degassed for 10 min under vacuum at 120°C , and
394 the flask was filled with N_2 and heated to 200°C . Cs-oleate (0.8 ml from the stock solution
395 prepared as described above) was swiftly injected when 200°C was reached. After 10 s the
396 reaction was stopped by cooling the reaction system with a water bath. The solution was
397 centrifuged (4 min, 13750 g) and the supernatant discarded. Hexane (0.3 ml) was added to
398 the precipitate to disperse the nanocrystals and centrifuged again. The obtained precipitate
399 was redispersed in 3 ml toluene and centrifuged (2 min, 2200 g). The supernatant was
400 separated from the precipitate, filtered, and used for our investigations. For CsPbBr_2Cl ,
401 0.094 mmol PbCl_2 , 0.282 mmol PbBr_2 , dried OA (1.5 ml), dried OAm (1.5 ml), TOP (1 ml), and
402 dried ODE (5 ml) were loaded into a 25-ml 3-neck flask and the same protocol was followed.

403 **Sample preparation.** For single-nanocrystal spectroscopy, the colloidal dispersions from the
404 above syntheses were diluted to nanomolar concentrations in solutions of 3 mass percent
405 polystyrene in toluene. This dispersion was then spin-casted at 5000 r.p.m. onto intrinsic
406 crystalline Si wafers with a 3- μm -thick thermal-oxide layer. For ensemble measurements, the
407 undiluted nanocrystal dispersions from the previous section were drop-casted on glass
408 substrates. For photoluminescence quantum-yield measurements, 0.1 ml of the colloidal
409 dispersion was mixed with 0.1 ml of a 5-mass-percent solution of poly(methyl methacrylate)
410 (PMMA, 495,000 molecular weight) in toluene.

411 **Optical characterization.** All optical measurements of single nanocrystals were performed in
412 a self-built micro-photoluminescence ($\mu\text{-PL}$) setup. The samples were mounted on xyz nano-
413 positioning stages inside an evacuated liquid-helium flow cryostat and cooled down to a
414 targeted temperature of 5 K (see Fig. 3 caption). Single nanocrystals were excited by means
415 of a fiber-coupled excitation laser at an energy of 3.06 eV with a repetition rate of 40 MHz and
416 a pulse duration of 50 ps. The excitation beam was sent through a linear polarizer and a
417 short-wavelength-pass filter before being directed toward the sample by a dichroic beam
418 splitter. Typical power densities used to excite single nanocrystals were 2-120 W/cm^2 .
419 Assuming an absorption cross section of $8 \times 10^{-14} \text{ cm}^2$ (ref. 31), this yields 0.0057-0.34
420 excitons per nanocrystal per pulse³². For both excitation and detection, a long-working
421 distance 100x microscope objective with numerical aperture of 0.7 was used. The nearly
422 Gaussian excitation spot had a $1/e^2$ diameter of 1.4 μm . The emission was filtered using a
423 long-pass filter and dispersed by a 0.75 m monochromator with an 1800 lines/mm grating
424 before detection with a back-illuminated, cooled charge-coupled device camera. For
425 polarization-dependent measurements, a liquid-crystal retarder was employed to compensate
426 for retardation effects in the setup. For photoluminescence lifetime and time-tagged time-

427 resolved (TTTR3) single-photon-counting measurements, we filtered the emission with a
428 suitable tunable bandpass filter to either measure only the excitonic photoluminescence
429 decay or to correlate excitonic and trionic emission intensities and decay times with a time-
430 correlated single-photon-counting system with nominal time resolution of 30 ps.

431 Ensemble measurements were performed in an exchange-gas cryostat at 5 K. Here, the
432 samples were excited with a frequency-doubled Ti:sapphire femtosecond pulsed laser with a
433 repetition rate of 80 MHz at 3.1 eV. Optical power densities were below 3 W/cm². The emitted
434 light was dispersed by a 150 lines/mm grating within a 300-mm focal length spectrograph and
435 detected by a streak camera with 2 ps resolution. Absolute photoluminescence quantum-yield
436 measurements at room temperature were performed on a Quantaurus QY (C11347-11,
437 Hamamatsu).

438 **Band-structure calculations.** Figure 1b and Extended Data Fig. 1 show calculated band
439 structures for CsPbBr₃, CsPbCl₃, and CsPbI₃. We assume that these materials exist in the
440 cubic perovskite structure with a lattice constant of 5.865, 5.610, and 6.238 Å, respectively³³.
441 The electronic structure of these crystals was determined using the Vienna *Ab-initio*
442 Simulation Package (VASP)³⁴⁻³⁶ with projector-augmented wavefunctions³⁷. Our initial
443 calculations used the PBEsol^{38,39} generalized gradient approximation, and included spin-orbit
444 coupling. We used an energy cutoff of 400 eV and Γ -centered k-point grid of 6×6×6, which
445 yield 40 k-points in the irreducible Brillouin zone.

446 As expected, standard density functional theory (DFT) seriously underestimates the
447 bandgap in these materials. Accordingly, we used a modified version of the Heyd-Scuseria-
448 Ernzerhof “HSE06” hybrid functional⁴⁰, which mixes exact Hartree-Fock exchange with
449 conventional DFT. We initially started with 25% mixing, and planned to adjust the mixing to
450 match the observed bandgap. However, this was not possible, even with 45% Hartree-Fock in

the calculation for CsPbBr₃. This produced a bandgap of 1.4 eV, far smaller than the experimental gap of 2.8 eV. Rather than using even higher mixing, or even a full-scale Hartree-Fock calculation, we instead added a scissors operator to adjust the bandgap to the experimental result. We found that the electron and hole masses were nearly unchanged with Hartree-Fock mixing, leading us to believe that this technique still provides the correct physics. Further confirmation was provided by conducting G_0W_0 calculations (also with VASP) on top of the PBE results. For this approach, we employed a plane-wave energy cutoff of 600 eV, a 150 eV energy cutoff for the response functions, 1894 unoccupied states, spin-orbit coupling, and “GW” pseudopotentials including all semicore electrons. Although these calculations yielded band gaps that were in closer agreement with experiment (1.96 eV for CsPbI₃, 2.36 eV for CsPbBr₃, and 3.27 eV for CsPbCl₃), other aspects of the band structure remained virtually unchanged.

Data availability. All data generated or analysed during this study are included in this published article (and its supplementary information files).

31. Yakunin, S., Protesescu, L., Krieg, F., Bodnarchuk, M. I., Nedelcu, G., Humer, M., De Luca, G., Fiebig, M., Heiss, W. & Kovalenko, M. V. Low-threshold amplified spontaneous emission and lasing from colloidal nanocrystals of caesium lead halide perovskites. **6**, 8056 (2015).
32. Smyder, J. A., Amori, S. R., Odoi, M. Y., Stern, H. A., Peterson, J. J. & Krauss, T. D. The influence of continuous vs. pulsed laser excitation on single quantum dot photophysics. *Phys. Chem. Chem. Phys.* **16**, 25723-25728 (2014).
33. Mehl, M. J., Hicks, D., Toher, C., Levy, O., Hanson, R. M., Hart, G. & Curtarolo, S. The AFLOW library of crystallographic prototypes. Preprint at <https://arxiv.org/abs/1607.02532> (2016).
34. Kresse, G., *Ab Initio* Molekular Dynamik für Flüssige Metalle, Ph.D. thesis, Technische Universität Wien, 1993.
35. Kresse, G. & Hafner, J. *Ab initio* molecular dynamics for open-shell transition metals. *Phys. Rev. B* **48**, 13115-13118 (1993).
36. Kresse, G. & Hafner, J. *Ab initio* molecular-dynamics simulation of the liquid-metal–amorphous-semiconductor transition in germanium. *Phys. Rev. B* **49**, 14251-14269 (1994).
37. Blöchl, P. E. Projector augmented-wave method. *Phys. Rev. B* **50**, 17953-17979 (1994).
38. Perdew, J. P., Ruzsinszky, A., Csonka, G. I., Vydrov, O. A., Scuseria, G. E., Constantin, L. A., Zhou, X. & Burke, K. Restoring the density-gradient expansion for exchange in solids and surfaces. *Phys. Rev. Lett.* **100**, 136406 (2008).

39. Perdew, J. P., Ruzsinszky, A., Csonka, G. I., Vydrov, O. A., Scuseria, G. E., Constantin, L. A., Zhou, X. & Burke, K. Erratum: Restoring the density-gradient expansion for exchange in solids and surfaces. *Phys. Rev. Lett.* **102**, 039902 (2009).
40. Krukau, A. V., Vydrov, O. A., Izmaylov, A. F. & Scuseria, G. E. Influence of the exchange screening parameter on the performance of screened hybrid functionals. *J. Chem. Phys.* **125**, 224106 (2006).

Extended Data Figure legends

Extended Data Figure 1 | Electronic structure for perovskite CsPbCl₃ and CsPbI₃. **a**, Calculated band structure of cubic perovskite CsPbCl₃. **b**, Calculated band structure of cubic perovskite CsPbI₃. See Methods for details about the calculations.

Extended Data Figure 2 | Measurements to estimate the low-temperature quantum-yield (QY) for our CsPbBr₂Cl nanocrystals. **a**, Photoluminescence spectra and **b**, decays for CsPbBr₂Cl nanocrystals ($L=14\pm1$ nm) embedded in a poly(methyl methacrylate) (PMMA) film at 295 and 5 K. For the same sample, a calibrated integrating sphere was used to measure the photoluminescence QY at 295 K ($43\pm1\%$). To obtain the QY at 5 K, the photoluminescence and optical absorption for several spots at 295 and 5 K under constant weak excitation (at 3.06 eV) were measured. The photoluminescence increased significantly, as seen in both the spectra and decay signal, while the absorption stayed nearly constant (data not shown). From these results, the QY at 5 K was estimated to be $88\pm14\%$. The photoluminescence decays in **b** are plotted both on a linear and logarithmic (inset) intensity scale with decay times of 1.60 (295 K) and 0.23 ns (5 K). The decrease in decay time at low temperature is clearly accompanied by an increase in the total emitted intensity (area under the decay traces).

Extended Data Figure 3 | Exciton and trion emission from an individual CsPbBr₂Cl nanocrystal. **a**, Photoluminescence spectrum of a single CsPbBr₂Cl nanocrystal showing two

509 exciton peaks at 2.5158 and 2.5175 eV and a trion peak that is red-shifted by 15-17 meV. The
510 targeted temperature was 5 K (see Fig. 3 caption). **b**, Polarization properties of the exciton
511 (left plot) and trion (right plot) emission peaks. The normalized area of a Lorentzian-peak fit
512 for two exciton peaks (red and blue) and the trion peak (black) are shown as a function of the
513 linear polarizer angle (placed in front of the spectrograph). Both exciton peaks show a
514 dominantly linear polarization, with the main axis being indicated by the blue and red lines.
515 The trion emission is unpolarized. See Supplementary Section 4 for further discussion.

516 **Extended Data Figure 4 | Composition-dependent ensemble photoluminescence decay**
517 **measurements of lead halide perovskite nanocrystals.** **a**, Typical streak-camera
518 measurement of the photoluminescence from an ensemble of CsPbBr₂Cl nanocrystals at 5 K.
519 In this example, the nanocrystals have $L=14$ nm. The emission peak is centered at 2.51 eV,
520 and the exponential decay time is 210 ps, as extracted by summing over all energies, which is
521 in good agreement with the results for single CsPbBr₂Cl nanocrystals of the same size. The
522 ensemble decay spectrum is slightly asymmetric (being faster at higher energies), which
523 might originate from the activation of an energy-transfer process from smaller to larger
524 nanocrystals. To account for the latter effect, we have only considered the long component of
525 the decay curve. **b**, Photoluminescence lifetimes at 5 K extracted for ensemble samples of
526 nanocrystals of various compositions and sizes. The ensemble data (solid circles) are
527 compared with single-nanocrystal measurements (open circles). The good agreement
528 between the two data sets is further evidence that the measured single-nanocrystal
529 photoluminescence decays are due to fast exciton radiative lifetimes and not due to trions, as
530 the ensemble data are acquired at very low excitation power where photo-generated charging
531 is not observed.

532 **Extended Data Figure 5 | Calculation of the interior electric field in cube-shaped**
533 **nanocrystals. a**, Line plot of the electric potential, ϕ , along the center line between the
534 capacitor plates (see Supplementary Section 3.B). **b**, Line plot of the normalized electric-field
535 magnitude, E_z^z/E_∞^z , along the center line between the capacitor plates.

536 **Extended Data Figure 6 | Contour plots of normalized electric-field magnitude across a**
537 **cube-shaped nanocrystal. a-d**, Contour plots of E_z^z/E_∞^z for four different ratios (4, 6, 8, and
538 10, respectively) of the dielectric constant inside the nanocrystal (ϵ_{in}) to the surrounding
539 medium (ϵ_{out}) (see Supplementary Section 3.B). The plots depict the xz mid-plane of the cube
540 and is valid for the symmetry-equivalent yz mid-plane. The z direction is vertical. **e**, Contour
541 plot of E_x^z/E_∞^z on the xz mid-plane of the cube. The ratio of ϵ_{in} to ϵ_{out} was set to 9. The E_y^z/E_∞^z
542 distribution on the yz mid-plane is identical. In all plots, the z direction is vertical, and the
543 perturbations near the corners of the plots are artifacts of the interpolation resolution utilized
544 by the software used to construct them.

545 **Extended Data Figure 7 | Extraction of the Kane energy, E_p , for the lead halide**
546 **perovskites.** From the band structures presented in Fig. 1b and Extended Data Fig. 1, the
547 Kane energy, defined according to equation (5) in the main text, can be extracted for
548 CsPbCl_3 , CsPbBr_3 , and CsPbI_3 from the band structure near the band edges. See
549 Supplementary Section 1.B for details.

550 **Extended Data Figure 8 | Calculations related to the determination of the exciton**
551 **radiative lifetime in cube-shaped nanocrystals within the intermediate-confinement**
552 **regime. a**, Dimensionless electron–hole correlation constant, $b=\beta L$, and **b**, the square
553 modulus of the ratio of $I_{||}$ for intermediate and strong confinement as a function of the size of
554 the nanocrystal relative to the electron Bohr radius, L/a_e , for the three materials studied. The

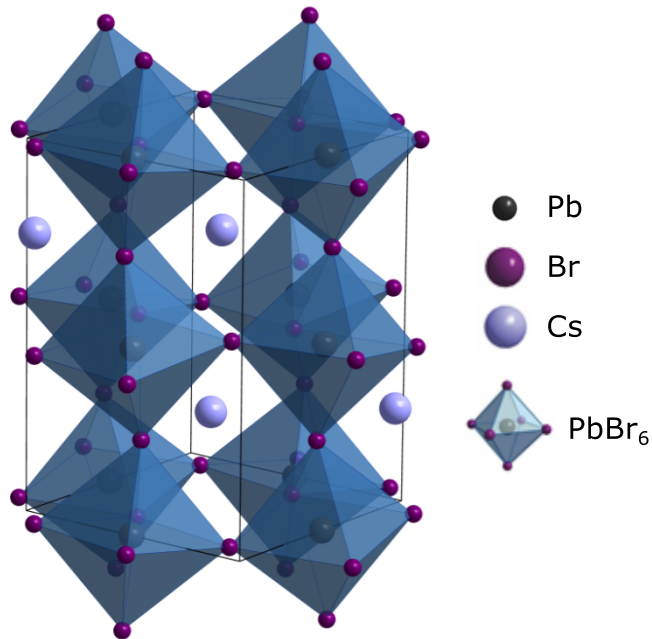
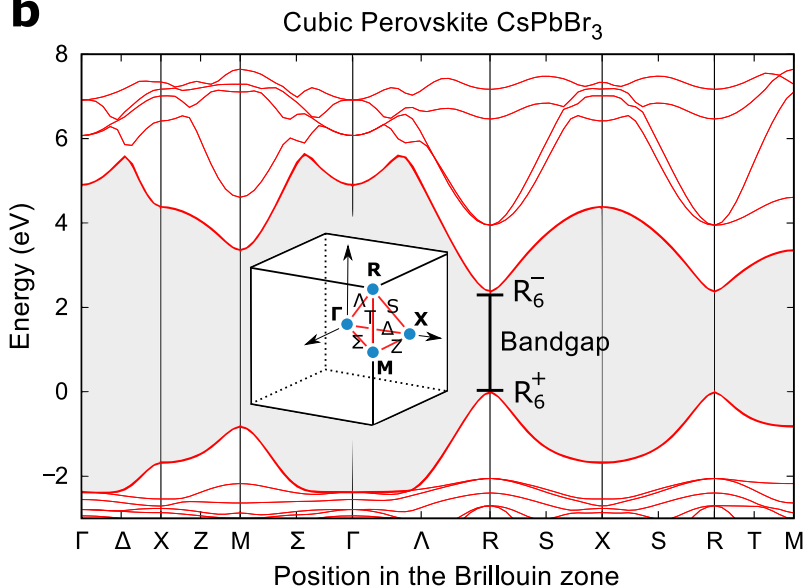
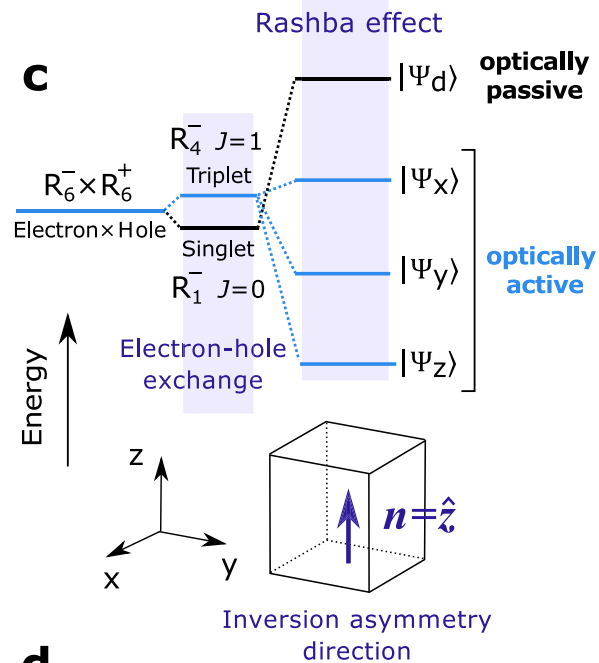
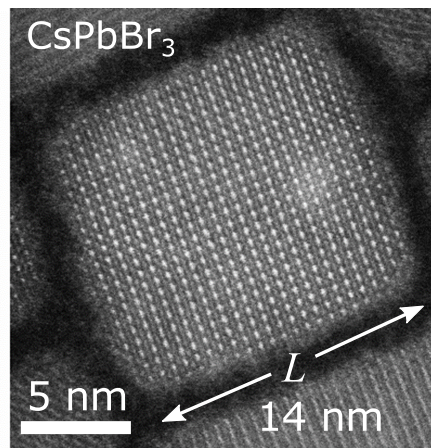
inset in **b** shows the square modulus of I_{\parallel} in the strong-confinement regime for several different dielectric constants, $\epsilon_{\text{in}}/\epsilon_{\text{out}}$. See Supplementary Section 3.D for details.

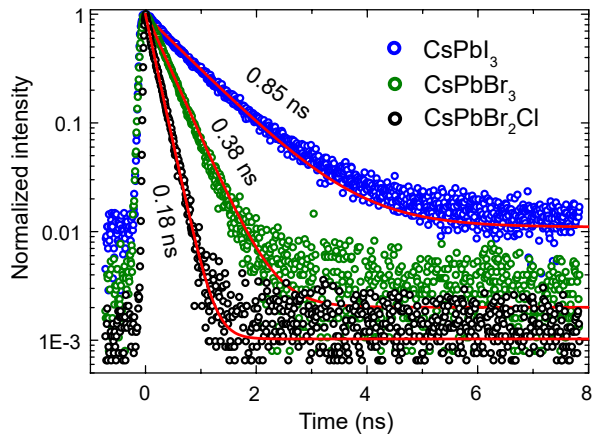
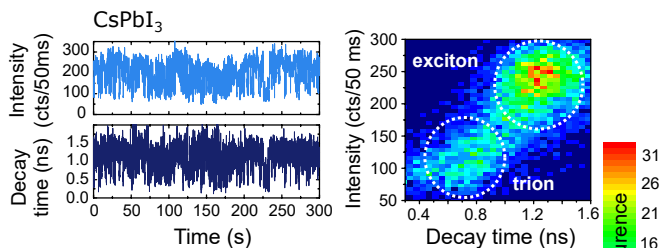
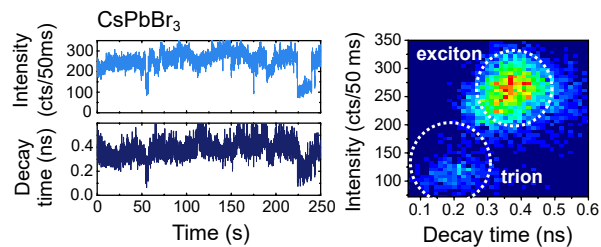
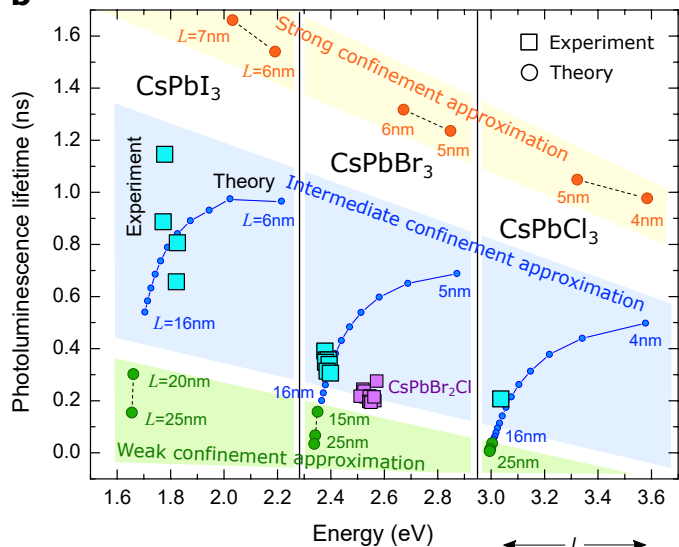
Extended Data Figure 9 | Representative 2-peak spectra for individual CsPbBr₂Cl nanocrystals. **a-i**, Photoluminescence spectra of single nanocrystals at a targeted temperature of 5 K (see Fig. 3 caption). Each spectrum was recorded with a linear polarizer in the detection path. Thus, the displayed relative intensities cannot be used to determine the relative (potentially thermal) population within the fine structure multiplet. The linear polarizer was used here because it can be rotated to resolve all spectral features. Without the polarizer, the low-energy peak typically dominates in intensity.

Extended Data Figure 10 | Representative 3-peak spectra for individual CsPbBr₂Cl nanocrystals. **a-i**, Photoluminescence spectra of single nanocrystals at a targeted temperature of 5 K (see Fig. 3 caption). Each spectrum was recorded with a linear polarizer in the detection path. Thus, the displayed relative intensities cannot be used to determine the relative (potentially thermal) population within the fine structure multiplet. The linear polarizer was used here because it can be rotated to resolve all spectral features. Without the polarizer, the low-energy peak typically dominates in intensity.

Extended Data Figure 11 | Predicted exciton spectra and polarization properties for individual perovskite nanocrystals. The plots show the expected exciton fine structure in photoluminescence spectra from three orthogonal dipoles of the lowest energy exciton. The dipoles are oriented along the orthorhombic symmetry axes. Each plot includes an inset with the emission probability for the dipoles as a function of the polarization angle. **a-d**, Expected fine structure for observation in the [010], [001], [011], and [312] directions with respect to the orthorhombic symmetry axes. The temperature effect on the population of the sublevels is not

578 considered (*i.e.*, the populations of the sublevels are assumed to be equal). **e-h**, Expected
579 fine structure for observation in the [010], [001], [011], and [312] directions with respect to the
580 orthorhombic symmetry axes. The temperature effect on the population of the sublevels is
581 considered. The temperature is assumed to be comparable to the fine-structure splitting, *i.e.*
582 $k_b T \approx \Delta_1 = \Delta_2$, where k_b is the Boltzmann constant and T is temperature. See Supplementary
583 Section 4 for further details.

a**b****c****d**

a**c****d****b****e**